High field effective linewidth and eddy current losses in moderate conductivity single crystal Zn-Y hexagonal ferrite at 10–35 GHz

John R. Truedson, Pavel Kabos,[a] Kevin D. McKinstry, and Carl E. Patton
Department of Physics, Colorado State University, Ft. Collins, Colorado 80523

(Received 2 September 1993; accepted for publication 15 March 1994)

The microwave losses associated with the extreme high field tail region of the ferromagnetic resonance (FMR) absorption curve for 0.08- to 1.38-mm-thick *c*-plane circular disks of single crystal Zn-Y hexagonal ferrite materials with planar anisotropy were investigated at 10, 19.3, and 35.3 GHz, with the static external magnetic field applied in plane. Analysis of the data in terms of magnetic losses only gave anomalous high field effective linewidth ΔH_F results; this ΔH_F showed a substantial increase with the field, changed with both disk thickness and radius, and was higher for an out-of-plane microwave field direction than for an in-plane direction. This linewidth did scale with the square of the disk thickness, one indication of predominant eddy current losses. The data were then analyzed in terms of eddy current losses, based on the assumption of an insulator FMR response and a high field eddy current loss absorption tail driven by that response. The predictions of the model were in good agreement with the data. Fits to the data gave reasonable and consistent values of the microwave conductivity which ranged from 0.03 to 0.05 $\Omega^{-1}\,\mathrm{cm}^{-1}$ at 10 GHz to 0.06–0.07 $\Omega^{-1}\,\mathrm{cm}^{-1}$ at 35 GHz, relative to a measured dc conductivity of 0.02–0.03 $\Omega^{-1}\,\mathrm{cm}^{-1}$.

I. INTRODUCTION

Off-resonance effective linewidth analysis techniques[1] to characterize the microwave losses in magnetic materials have been used in the past to study loss processes in hexagonal ferrites.[2–4] Recently, the technique has been adapted to study off-resonance microwave and millimeter wave losses due to eddy currents in moderate conductivity Ba-M type hexagonal ferrite with uniaxial magnetic anisotropy.[5,6] The analysis was based on a model in which the insulator ferromagnetic resonance (FMR) response generates eddy currents[7,8] and produces an FMR absorption tail due to these eddy current losses. An eddy current tail (ECT) response analysis was developed to analyze the eddy current losses by *means* of a linear fitting procedure in much the same way that the high field effective linewidth analysis of magnetic losses yields an effective linewidth. The ECT analysis yields a determination of the microwave conductivity.

The ECT analysis discussed in Ref. 6 was for *c*-plane barium ferrite disks magnetized along the easy axis and perpendicular to the disk plane. In that case, the analysis is simplified considerably because of the circular precession nature of the magnetic response. The analysis is more complicated for in-plane magnetized easy plane hexagonal ferrites because of the in-plane static magnetization configuration and the elliptical precession dynamic response. The focus of this work was on the off-resonance microwave and millimeter wave eddy current losses for in-plane magnetized moderate conductivity hexagonal ferrite Zn-Y disk samples with easy plane magnetocrystalline anisotropy.

In the first part of the work, the standard effective linewidth technique for moderate conductivity ferrites was used to determine the high field effective linewidth for *c*-plane disk samples of single crystal easy plane Zn-Y materials at 10.0, 19.3, and 35.3 GHz with the static magnetic field in plane and with the external microwave field either in plane or perpendicular to the disk plane. The high field effective linewidths obtained from these measurements were far from the usual result of a field independent and thickness independent linewidth parameter representative of intrinsic losses. Instead, these effective linewidths showed very strong and unexpected field dependences, changed with the orientation of the microwave field in plane or out of plane, increased as the square of the disk thickness, and also changed with disk diameter. As for the Ba-M hexagonal ferrite results in Refs. 5 and 6, the scaling of high field effective linewidths with the square of the disk thickness indicates that the predominant losses are due to eddy currents.

In the second part of the work, an ECT analysis technique was developed to analyze these Zn-Y disk measurements. The analysis parallels the approach in Ref. 6. The ECT analysis for the in-plane magnetized easy plane Zn-Y disk geometry, however, is quite different from the Ref. 6 analysis for uniaxial *c*-plane Ba-M disks magnetized perpendicular to the disk plane and with the microwave field always in plane. In the Zn-Y case, the eddy current distribution depends on both disk thickness and disk diameter. Once the basic eddy current response is obtained, the ECT analysis allows one to analyze the eddy current losses associated with the high field tail of the FMR absorption curve and use the microwave and millimeter wave data to determine the microwave conductivity versus frequency. For the present series of materials, the measured microwave conductivity increases linearly with frequency and extrapolates to dc values at low frequency.

[a]On leave of absence from Faculty of Electrical Engineering, Slovak Technical University, Bratislava, Slovakia.

 0021-8979/94/76(1)/432/11/$6.00 © 1994 American Institute of Physics

Downloaded 26 Dec 2001 to 129.82.140.114. Redistribution subject to AIP license or copyright, see http://ojps.aip.org/japo/japcr.jsp

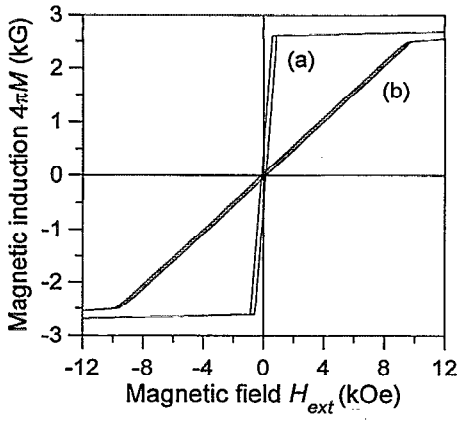

FIG. 1. Hysteresis curves of magnetic induction $4\pi M$ vs static external magnetic field H_{ext} for a single crystal Zn-Y hexagonal ferrite c-plane disk with a diameter of 3.0 mm and thickness of 0.89 mm. Curves (a) and (b) are for in-plane and perpendicular-to-plane magnetic field directions, respectively.

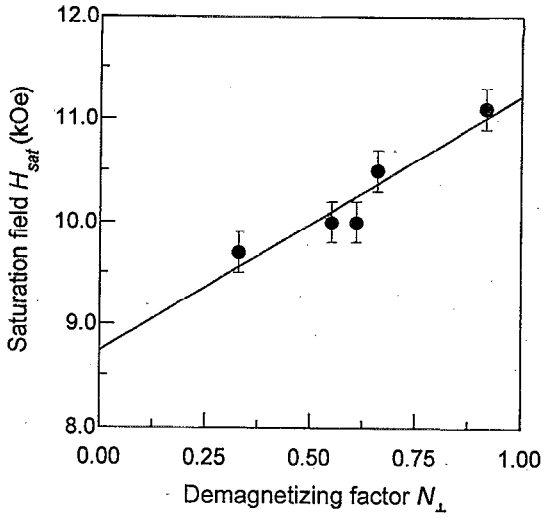

FIG. 2. Plot of the measured perpendicular-to-plane saturation field H_{sat} vs the perpendicular-to-plane demagnetizing factor $N_\perp$ for the four disk and one sphere single crystal Zn-Y samples. The solid line represents a linear best fit to the data.

II. MATERIALS, PROPERTIES, AND MICROWAVE MEASUREMENTS

The Zn-Y single crystals were prepared at Purdue University by a flux melt growth method.[9] Lapidary techniques were used to fabricate thin c-plane disks. The disk thicknesses ranged from 0.05 to 1.38 mm. Disk diameters ranged from 1 to 3 mm.

The static magnetic properties of four disk samples of various thicknesses and one sphere sample were characterized by vibrating sample magnetometry. Hysteresis curves of the magnetic induction $4\pi M$ versus static external magnetic field H_{ext} were measured for both in-plane and perpendicular-to-plane field directions. Here, "plane" refers both to the disk plane and the crystallographic c plane. Values for the saturation induction $4\pi M_s$ and the anisotropy field H_A were determined from these data. An example of such a hysteresis curve set is shown in Fig. 1 for an 0.89-mm-thick, 3.0-mm-diam disk. The in-plane field curve is labeled (a) in Fig. 1. The perpendicular-to-plane field curve is labeled (b). Note that the saturation magnetization $4\pi M_s$ apparent from curve (a) for the easy direction is slightly larger than the value obtained from curve (b) for the hard direction. This discrepancy is not understood. The average $4\pi M_s$ value from all the data for the five samples was 2.70 kG. Turn now to the saturation fields. Curve (a) clearly saturates at lower fields than does curve (b), as expected for disks with easy plane anisotropy. The curve (b) saturation field H_{sat} for this disk is about 9 kOe. These H_{sat} values ranged from 9.6 to 11.2 kOe. Thinner disks generally had larger H_{sat} values.

The perpendicular-to-plane field direction hysteresis curve H_{sat} values were used to determine the anisotropy field H_A. This anisotropy field is defined in terms of the usual uniaxial anisotropy energy density parameter K_u by the relation $H_A=2|K_u|/M_s$. The anisotropy field H_A was obtained by plotting the measured perpendicular-to-plane H_{sat} values versus the perpendicular-to-plane disk demagnetizing factor $N_\perp$ and extrapolating the data to the value of H_{sat} in the limit $N_\perp=0$. This procedure parallels the procedure used for the Ba-M ferrite disks in Ref. 6. In that case, H_{sat} was measured for the in-plane field direction and plotted against the in-plane demagnetizing factor $N_\parallel$. This procedure can be justified on the basis of a simple domain rotation model and the same argument discussed in Ref. 6. For a disk made up of narrow stripe domains, the saturation field H_{sat} perpendicular to the disk should decrease with increasing disk thickness according to

$$H_{sat}=H_A+4\pi M_s N_\perp . \tag{1}$$

From Eq. (1), the intercept of the fitted line in Fig. 2 with the vertical H_{sat} axis should correspond to the intrinsic anisotropy field H_A. The slope of the fitted line should correspond to the saturation induction $4\pi M_s$.

Figure 2 shows a plot of the measured out-of-plane saturation field H_{sat} for the four disk samples and the sphere as a function of the demagnetizing factor $N_\perp$. The straight line shows a straight line best fit to the data. The $N_\perp$ parameters were obtained from the disk sample dimensions, the ellipsoidal sample approximation, and the work of Osborn.[10] The point at $N_\perp=1/3$ is for the sphere. The extrapolated value of H_{sat} at $N_\perp=0$ is 8.75 ± 0.20 kOe. As indicated above, this intercept gives H_A. This $H_A=8.75$ kOe value is at the lower end of the range of H_A values usually cited for Zn-Y.[11] The slope of the fitted line is 2.6 ± 0.2 kG. This slope is reasonably close to $4\pi M_s$, as expected from Eq. (1).

The microwave and millimeter wave cavity measurements were made for the thin disk samples described above at nominal frequencies of 10.0, 19.3, and 35.3 GHz. The measurements were of the cavity frequency ω and cavity quality factor Q versus the in-plane static external field H_{ext} for the range 3–11 kOe at 10.0 GHz, 5–13 kOe at 19.3 GHz, and 10–15 kOe at 35.3 GHz. The lower field limit was chosen to ensure saturated materials, based on the hysteresis curve data, and magnetic fields which are well above the

Downloaded 26 Dec 2001 to 129.82.140.114. Redistribution subject to AIP license or copyright, see http://ojps.aip.org/japo/japcr.jsp

FMR field. The measurements were done for two different linearly polarized microwave field configurations, a "P" configuration with the microwave field perpendicular to the disk plane and an "I" configuration with the microwave field in the disk plane and perpendicular to the static field. In a typical measurement a disk sample is mounted in the center of a TE_{011} cylindrical microwave cavity, which is centered in the gap of an electromagnet. The external magnetic field H_{ext} is applied parallel to the disk plane and in the easy crystallographic c-plane direction for the sample. With proper sample mounting, the linearly polarized microwave field may be either parallel or perpendicular to the disk plane. Cavity resonance frequency ω and quality factor Q measurements are then made as a function of H_{ext}. All measurements were made at room temperature.

These cavity data were then analyzed in two different ways. The first approach was in terms of the usual microwave susceptibility and magnetic losses. This procedure gives a measure of the losses in terms of a field dependent high field effective linewidth.[1] This approach and the results of the analysis for the Zn-Y disks are presented in Sec. III. As already indicated, the effective linewidth analysis revealed significant problems, mainly in terms of a linewidth parameter which depended on the static field and the microwave configuration as well as the disk thickness and diameter. The complicating factor is in the moderate conductivity and dominant effect of eddy current losses on the FMR absorption tail. The second approach, therefore, was to analyze the same data in terms of eddy current losses. This approach and the results of the analysis are described in Secs. IV and V.

III. EFFECTIVE LINEWIDTH ANALYSIS

As briefly described in the previous section, microwave cavity measurements of the microwave response of ferrites at fields well above the FMR field can be used to determine an off-resonance loss parameter known as the effective linewidth. This section briefly describes the effective linewidth technique for the specific situation of planar single crystal hexagonal ferrite c-plane disks magnetized to saturation by an in-plane static external field, and presents the results of a corresponding analysis of the Zn-Y disk data. The magnetic response equations and the basic high field fitting procedure given below will also be used for the ECT analysis of the next section.

The analysis is similar to that described in Ref. 6. The starting point is the connection between the microwave tensor susceptibility components of the ferrite sample and the various material and experimental parameters. Consider an easy plane hexagonal ferrite single crystal magnetic sample in the form of a circular disk with its axis along the crystallographic c axis and magnetized to saturation in the plane of the disk by a static external magnetic field H_{ext}. Figure 3 shows a diagram of the sample and magnetization-field geometry for a disk of thickness T and radius R. The disk is magnetized to saturation in the direction parallel to the disk plane by the static magnetic field $\mathbf{H}_{ext}$. The vector saturation magnetization $\mathbf{M}_s$ is parallel to $\mathbf{H}_{ext}$. Note that the x, y, and z axes of the defined x-y-z coordinate system are perpendicular to the disk, in plane but perpendicular to $\mathbf{M}_s$ and $\mathbf{H}_{ext}$, and along $\mathbf{M}_s$ and $\mathbf{H}_{ext}$, respectively. The vectors $\mathbf{h}_P$ and $\mathbf{h}_I$ directed along the x and y axes represent the perpendicular-to-plane (P) and in-plane (I) microwave field configurations already discussed. This P and I notation will be used throughout the remainder of this article to designate the two microwave configurations. In the experiment, only *one* of these fields will be present at a time. The ellipse circumscribed in the disk cross section and the $\mathbf{m}$ vector indicates the microwave magnetization response induced by $\mathbf{h}_P$ or $\mathbf{h}_I$. The diagram at the bottom of Fig. 3 shows two additional axes in the y-z plane, an r and a ϕ axis. The (r,ϕ,x) coordinate system will be useful for the eddy current analysis of Sec. IV.

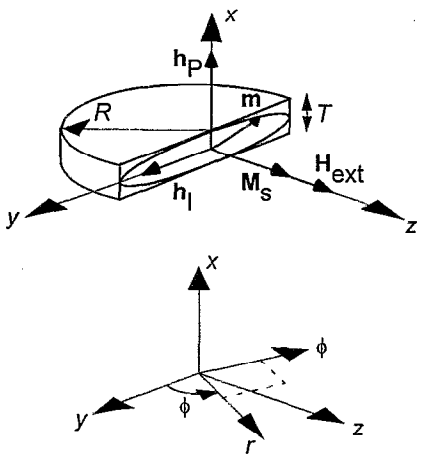

FIG. 3. Diagrams of the disk (x,y,z) coordinate system for a ferrite disk of thickness T and radius R and the (r,ϕ,x) coordinate system for the eddy current problem. The disk is centered at $x=0$ and is perpendicular to the x axis. The in-plane magnetic field $\mathbf{H}_{ext}$ and the static magnetization $\mathbf{M}_s$ are along the z axis. The dynamic magnetization $\mathbf{m}$ describes a precession ellipse which is perpendicular to the z axis. The (r,ϕ,x) coordinate system has the r axis in the disk plane and at an angle ϕ relative to the positive y axis and a ϕ axis at ϕ relative to the positive z axis.

In order to analyze the magnetic response, one assumes a low amplitude microwave field $\mathbf{h}(t)=\mathbf{h}e^{i\omega t}$ of frequency ω which produces a dynamic magnetization response $\mathbf{m}(t)=\mathbf{m}e^{i\omega t}$. The vector $\mathbf{h}$ denotes the microwave field and $\mathbf{m}$ denotes the complex dynamic magnetization response. Low power levels and the condition $|\mathbf{m}|\ll M_s$ are assumed. If the vector magnetization $\mathbf{M}$ is taken as constant at $|\mathbf{M}|=M_s$, to lowest order $\mathbf{m}$ has only x and y components. The dynamic linear response can then be obtained directly from the magnetic torque equation of motion in the form $4\pi\mathbf{m}=4\pi\chi\cdot\mathbf{h}$,[12]

$$\begin{pmatrix} 4\pi m_x \\ 4\pi m_y \end{pmatrix} = \begin{pmatrix} 4\pi\chi_x & -i4\pi\kappa \\ i4\pi\kappa & 4\pi\chi_y \end{pmatrix} \begin{pmatrix} h_x \\ h_y \end{pmatrix}. \tag{2}$$

For a microwave field of amplitude h, the $\mathbf{h}_P$ field defined above has $h_x=h$ and $h_y=0$, while $\mathbf{h}_I$ has $h_x=0$ and $h_y=h$.

The susceptibility components $4\pi\kappa$, $4\pi\chi_x$, and $4\pi\chi_y$ can be separated into real and negative imaginary parts as $4\pi\chi_{x,y}=4\pi\chi'_{x,y}-i4\pi\chi''_{x,y}$ and $4\pi\kappa=4\pi\kappa'-i4\pi\kappa''$. For this work the analysis is limited to static external fields very

Downloaded 26 Dec 2001 to 129.82.140.114. Redistribution subject to AIP license or copyright, see http://ojps.aip.org/japo/japcr.jsp

far from ferromagnetic resonance. In this far field regime, the $4\pi\chi'_{x,y}$, $4\pi\chi''_{x,y}$, $4\pi\kappa'$, and $4\pi\kappa''$ response terms may be written as

$$4\pi\chi'_{x,y}=\frac{4\pi M_s H_{Y,X}}{[H_0^2-(\omega/|\gamma|)^2]}, \tag{3}$$

$$4\pi\chi''_{x,y}=\frac{1}{2}\frac{4\pi M_s\Delta H_F[H_{Y,X}^2+(\omega/|\gamma|)^2]}{[H_0^2-(\omega/|\gamma|)^2]^2}, \tag{4}$$

$$4\pi\kappa'=-\frac{4\pi M_s(\omega/|\gamma|)}{[H_0^2-(\omega/|\gamma|)^2]}, \tag{5}$$

and

$$4\pi\kappa''=\frac{1}{2}\frac{4\pi M_s\Delta H_F(H_X+H_Y)(\omega/|\gamma|)}{[H_0^2-(\omega/|\gamma|)^2]^2}. \tag{6}$$

In the above, H_X and H_Y are effective stiffness fields for the out-of-plane and in-plane tipping of the magnetization vector **M**.

$$H_X=H_{\text{ext}}+H_A+4\pi M_s(N_\perp-N_\parallel), \tag{7}$$

$$H_Y=H_{\text{ext}}. \tag{8}$$

The H_X stiffness field reflects the effect of both the planar anisotropy and the disk demagnetizing factors to keep the overall magnetization vector **M** in the plane of the disk. When the **M** tipping is in plane, only the static external magnetic field contributes to the effective stiffness field H_Y. The H_0 parameter is the geometric mean of the H_X and H_Y fields, according to $H_0=(H_XH_Y)^{1/2}$. The condition $H_0=\omega/|\gamma|$ corresponds to ferromagnetic resonance. The parameter γ is the electron gyromagnetic ratio. For Zn-Y materials, and given in practical units, $|\gamma|$ is close to 2.8 GHz/kOe. The corresponding values of H_{ext} for ferromagnetic resonance at the operating frequencies of 10.0, 19.3, 35.5 GHz pertinent to this work are 1.1, 3.4, and 8.4 kOe, respectively. The H_{ext} values for the current measurements are well above these FMR field values. The remaining parameter in Eqs. (3)–(6), ΔH_F, is the high field effective linewidth. As discussed in Refs. 1 and 6, this linewidth parameter expresses the applicable magnetic relaxation rate at a given field in linewidth units.

The $4\pi\chi'_{x,y}$, $4\pi\chi''_{x,y}$, $4\pi\kappa'$, and $4\pi\kappa''$ parameters play different roles in the microwave response of a ferrite. In the case of linear polarized microwave excitation, the FMR absorption curve of microwave loss versus frequency or field follows the functional form of the near-resonance $4\pi\chi''_{x,y}$ response, in the form of a Lorentzian curve with some half-power linewidth ΔH. This linewidth will be on the same order of or greater than the high field effective linewidth parameter ΔH_F, depending on the physical origin of the magnetic losses at resonance. From the high field perspective, ΔH_F should represent the intrinsic magnetic losses of the material and be independent of the sample geometry and field. The high field loss tail of the FMR curve, moreover, will be evident as a decrease in $1/Q$ for the cavity containing the sample as the field is increased. This change in $1/Q$ should scale with H_{ext} according to Eq. (4).

In the same way that absorption and losses are connected to $4\pi\chi''_{x,y}$, dispersion effects are connected to $4\pi\chi'_{x,y}$. For the measurement process of Sec. II with a linearly polarized microwave field, the change in cavity frequency with field scales with the $4\pi\chi'_{x,y}$ tail response of Eq. (3). The $4\pi\kappa'$, and $4\pi\kappa''$ terms play no role in the FMR or tail response for a linearly polarized microwave field excitation. These terms will be important, however, for the eddy current analysis of the next section.

The far field effective linewidth ΔH_F is obtained from determinations of the $4\pi\chi'_{x,y}$ and $4\pi\chi''_{x,y}$ tail responses for high fields which are well above the FMR field. These determinations, in turn, are obtained from measurements of cavity Q and ω versus field. The connections between $4\pi\chi'_{x,y}$ and frequency and between $4\pi\chi''_{x,y}$ and Q are obtained from microwave cavity perturbation theory.[13]

$$\frac{\omega(H_{\text{ext}})-\omega_N}{\omega(H_{\text{ext}})}=-K_{\text{cav}}4\pi\chi'_{x,y}(H_{\text{ext}}), \tag{9}$$

$$\left(\frac{1}{Q(H_{\text{ext}})}-\frac{1}{Q_N}\right)=2K_{\text{cav}}4\pi\chi''_{x,y}(H_{\text{ext}}). \tag{10}$$

The frequency, quality factor, $4\pi\chi'_{x,y}$, and $4\pi\chi''_{x,y}$ terms in Eqs. (9) and (10) include explicit H_{ext} dependences. The Q and ω parameters depend on H_{ext} through the measurements and the $4\pi\chi'_{x,y}$ and $4\pi\chi''_{x,y}$ terms depend on H_{ext} through Eqs. (3) and (4). The ω_N and Q_N parameters represent limiting values of $\omega(H_{\text{ext}})$ and $Q(H_{\text{ext}})$ for very high field, in the limit of no magnetic interactions. As will be evident from Sec. IV, Q_N can contain contributions from eddy current losses in the sample if such losses are significant. The K_{cav} parameter is a calibration factor from the perturbation theory which depends on the cavity and the sample volume. In the present procedure, K_{cav} is obtained empirically.

The right-hand side of Eq. (9) gives a choice between $4\pi\chi'_x$ and $4\pi\chi'_y$, and Eq. (10) gives a choice between $4\pi\chi''_x$ and $4\pi\chi''_y$. The selection of $4\pi\chi'_x$ and $4\pi\chi''_x$ or $4\pi\chi'_y$ and $4\pi\chi''_y$ depends on the microwave field direction in the experiment. For the perpendicular to disk or P case, one uses $4\pi\chi'_x$ and $4\pi\chi''_x$. For the in plane or I case, one uses $4\pi\chi'_y$ and $4\pi\chi''_y$.

The above equations, in combination with the explicit expressions for $4\pi\chi'_{x,y}$ and $4\pi\chi''_{x,y}$ from Eqs. (3) and (4), yield two operational relations which may be used in conjunction with the $\omega(H_{\text{ext}})$ and $Q(H_{\text{ext}})$ measurements to determine directly the far-field effective linewidth ΔH_F. The $\omega(H_{\text{ext}})-4\pi\chi'_{x,y}$ connection from Eqs. (3) and (9) is given by

$$\omega(H_{\text{ext}})-\omega_N=-K_{\text{cav}}X_{FI,FP}, \tag{11}$$

where $X_{FI,FP}$ is given by

$$X_{FI,FP}=\omega\frac{4\pi M_s H_{X,Y}}{[H_0^2-(\omega/|\gamma|)^2]}. \tag{12}$$

Recall that $H_{X,Y}$ and H_0 are explicit functions of H_{ext} and that ω is also measured as a function of H_{ext}. This means that plots of the measured values of $\omega(H_{\text{ext}})$ vs X_{FI} for the I microwave configuration or of $\omega(H_{\text{ext}})$ vs X_{FP} for the P configuration should correspond to straight lines. It is to be

Downloaded 26 Dec 2001 to 129.82.140.114. Redistribution subject to AIP license or copyright, see http://ojps.aip.org/japo/japcr.jsp

emphasized that two sets of $\omega(H_{\text{ext}})$ measurements are involved, one for the I microwave field configuration with $\mathbf{h}=\mathbf{h}_I$ and one for the P microwave field configuration with $\mathbf{h}=\mathbf{h}_P$. The two straight line plots should have common slopes equal to $-K_{\text{cav}}$ and common vertical intercepts of ω_N. The extent to which the two plots give straight lines with common slopes and intercepts provides a good test of the validity of the off-resonance dispersion response equations.

The corresponding $Q(H_{\text{ext}}) - 4\pi\chi''_{x,y}$ connection from Eqs. (4) and (10) is given by

$$\left(\frac{1}{Q(H_{\text{ext}})}-\frac{1}{Q_N}\right)=+K_{\text{cav}}\Delta H_F\, X_{QI,QP}, \tag{13}$$

where $X_{QI,QP}$ is given by

$$X_{QI,QP}=\frac{4\pi M_s[H^2_{X,Y}+(\omega/|\gamma|)^2]}{[H^2_0-(\omega/|\gamma|)^2]^2}. \tag{14}$$

Note that $X_{QI,QP}$ has units of inverse field. In parallel with the above discussion for plots of $\omega(H_{\text{ext}})$ vs X_{FI} and $\omega(H_{\text{ext}})$ vs X_{FP}, plots of the measured values of $1/Q(H_{\text{ext}})$ vs X_{FI} for the I microwave configuration or of $1/Q(H_{\text{ext}})$ vs X_{FP} for the P configuration should also give to straight lines. In this case, the two lines should have a common slope equal to $+K_{\text{cav}}\Delta H_F$ and a common vertical intercept of $1/Q_N$. The extent to which the experimental plots give straight lines with common slopes and intercepts will provide a good test of the validity of the off-resonance absorption response equations for a fixed value of ΔH_F.

The final step in the analysis is to obtain values of ΔH_F at high field. In the barium ferrite work in Ref. 6, the analysis for individual disks gave the expected straight lines for both the ω plots and the $1/Q$ plots. It was possible, therefore, to obtain a *single* high field value for ΔH_F for each sample simply by taking the ratio of the slope of the $1/Q$ plot to the slope of the ω plot. This ΔH_F value, however, was then found to scale with the square of the disk thickness. This showed that ΔH_F was not a measure of the intrinsic magnetic losses of the materials. As shown in Ref. 6, the scaling was shown to be due to the dominant effect of eddy current losses in determining the tail FMR absorption response.

As will be evident from the results presented below, the situation for c-plane disks with planar anisotropy and in-plane fields is somewhat different. While the ω plots are quite linear and consistent with the response analysis given so far, $1/Q$ plots are not linear at all. In this situation, it is necessary to use the ω plots to determine K_{cav} alone, and then use Eqs. (13) and (14) at each value of H_{ext} used for the measurements to obtain a field dependent ΔH_F. Just as the change in ΔH_F with disk thickness for the barium ferrite measurements in Ref. 6 served as an indication that the origin of the FMR tail response was connected with eddy currents and not magnetic relaxation processes, the field dependent ΔH_F parameter for the present Zn-Y disks also has origins in eddy current losses. The rest of this section presents representative results on ΔH_F. Section IV summarizes the analysis of the FMR tail response explicitly in terms of eddy currents.

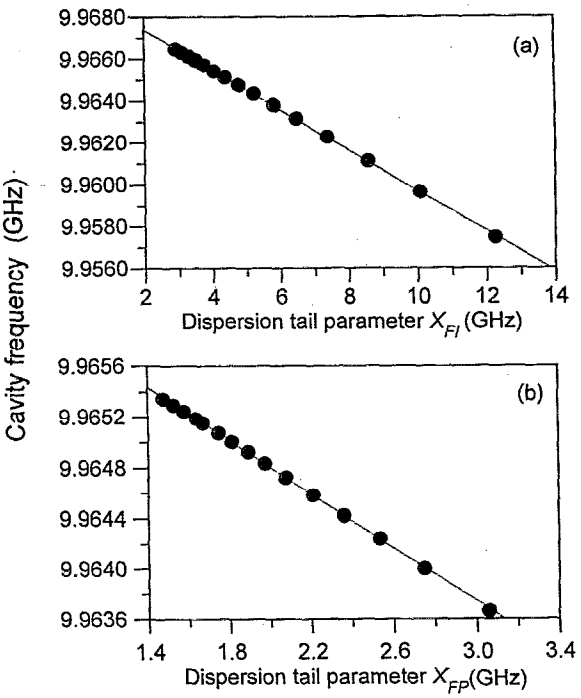

FIG. 4. Plots of measured cavity frequency vs the off-resonance dispersion tail X parameters X_{FI} and X_{FP} for the 10 GHz cavity and one particular single crystal c-plane Zn-Y disk sample with a thickness of 1.14 mm and a diameter of 3.0 mm: The static external magnetic field was in-plane. For (a), the microwave field was in plane and perpendicular to the static field. For (b), the microwave field was perpendicular to the disk plane. The solid lines represent linear best fits to the data.

Representative plots of the measured frequency $\omega(H_{\text{ext}})$ vs X_{FI} and $\omega(H_{\text{ext}})$ vs X_{FP} are shown in Fig. 4. The measurements were for a Zn-Y disk with a thickness of 1.14 mm and a diameter of 3.0 mm, with the 10 GHz cavity. Note again that two sets of $\omega(H_{\text{ext}})$ measurements are involved, one for the I microwave field configuration and one for the P configuration. The numerical values for the plotted X_{FI} and X_{FP} parameters were obtained from Eq. (12), the set of H_{ext} values used for the I or P cases, the corresponding measured $\omega(H_{\text{ext}})$ values, values for $N_{\parallel}$ and $N_{\perp}$ of 0.20 and 0.60, respectively, and values for the various Zn-Y materials parameters already listed.

Figure 4(a) is for the I configuration and Fig. 4(b) is for the P configuration. Both plots are quite linear. The slopes of the fitted lines in Figs. 4(a) and 4(b) are $(-9.63\pm0.4)\times10^{-4}$ and $(-10.6\pm0.4)\times10^{-4}$. Since both slopes should correspond to $-K_{\text{cav}}$, the slightly different values indicate that the calibration parameter is slightly different for the two disk orientations in the TE_{011} microwave cavity. The difference is about 10%. These slopes are also within 10% of the cavity calibration parameter obtained from perturbation theory. Similar results were obtained for other disk thicknesses and diameters and the other frequencies. Considered as a whole, the frequency versus field measurements were all in good agreement with the dispersion analysis of this section.

Representative plots of $1/Q(H_{\text{ext}})$ vs X_{QI} and $1/Q(H_{\text{ext}})$ vs X_{QP} from the Q vs H_{ext} measurements for the same disk

Downloaded 26 Dec 2001 to 129.82.140.114. Redistribution subject to AIP license or copyright, see http://ojps.aip.org/japo/japcr.jsp

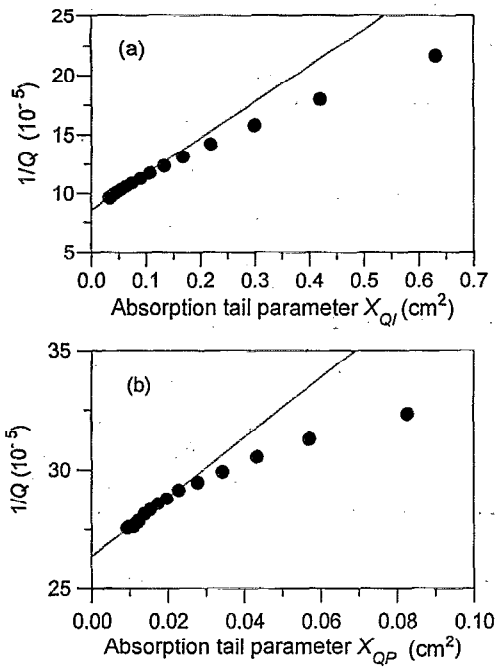

FIG. 5. Plots of $1/Q$ vs the off-resonance absorption tail X parameters X_{QI} and X_{QP} for the 10 GHz cavity and the same 1.14-mm-thick and 3.0-mm-diam single crystal c-plane Zn-Y disk used for Fig. 4. The static external magnetic field was in-plane. For (a), the microwave field was in plane and perpendicular to the static field. For (b), the microwave field was perpendicular to the disk plane. The solid lines represent linear best fits to the low X_{QI} and X_{QP} regions of the plots.

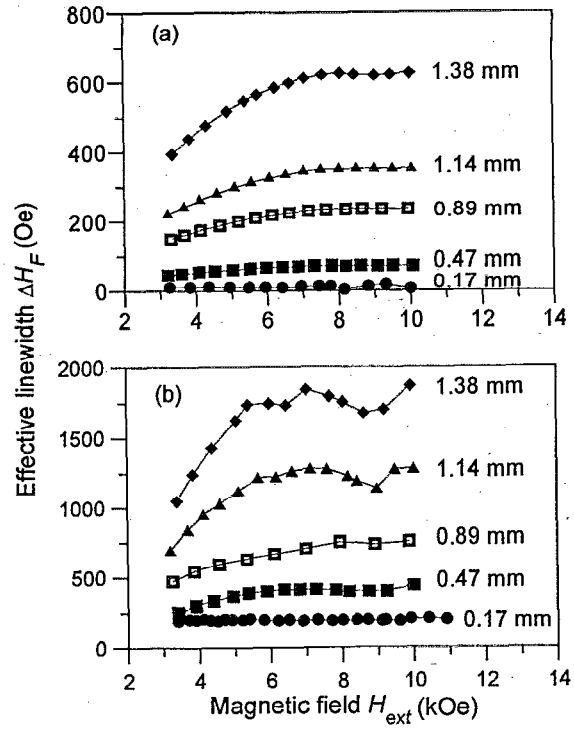

FIG. 6. Plots of the field dependent effective linewidth $\Delta H_F(H_{ext})$ at 10 GHz vs in-plane static external magnetic field H_{ext} for five single crystal Zn-Y disks with nominal diameters of 3 mm and thicknesses as indicated. The results in (a) are for the I configuration with the microwave field in plane. The results in (b) are for the P configuration with the microwave field perpendicular to the disk plane. The solid lines simply connect the data points.

in the I and P configurations are shown in Fig. 5. The numerical values for the plotted X_{QI} and X_{QP} parameters were obtained from Eq. (14), the two sets of H_{ext} and $\omega(H_{ext})$ values from the I or P experiments, and the other parameters already listed. Figure 5(a) is for the I configuration and Fig. 5(b) is for the P configuration. In contrast with the linear plots in Fig. 4, these plots are not linear at all, except for the lowest values of X_{QI} and X_{QP} shown. Note that these low X_{QI} and X_{QP} correspond to relatively high fields, with H_{ext} above 8–9 kOe or so. This means that the assumption of a single fixed high field effective linewidth is incorrect. Moreover, even if one uses the high field linear regions, the slopes of these limited range linear responses are quite different. The straight lines in Figs. 5(a) and 5(b) indicate linear best fits to the high field points. The slopes of the lines are (324 ± 9) and $(1210\pm50)\times10^{-4}$ Oe for Figs. 5(a) and 5(b), respectively. If these (a) and (b) slopes are divided by the K_{cav} values from Figs. 4(a) and 4(b), respectively, one obtains very different high field limiting values for ΔH_F. These limiting values are $\Delta H_F = 350\pm20$ Oe for the I measurements and $\Delta H_F = 1250\pm50$ Oe for the P measurements. From this factor-of-four difference, it is clear that even in the limit of very high fields and low X_{QI} and X_{QP} values where the plots are linear, ΔH_F still depends on the microwave field direction.

As already discussed, one can also take the K_{cav} values for the I and P measurements and use Eqs. (13) and (14) to obtain point by point values of ΔH_F as a function of H_{ext}. The results for this procedure, applied to the 10 GHz data for five disks with nominal 3 mm diam and different thicknesses as indicated, are shown in Fig. 6. The results in Fig. 6(a) are for the I microwave field configuration and Fig. 6(b) is for the P microwave field configuration. These results show that ΔH_F changes with (i) the static field H_{ext}, (ii) the microwave field orientation, and (iii) the disk thickness. The increase in ΔH_F with field is the same as noted in Ref. 4 for Zn-Y. Such an increase is peculiar. Any intrinsic high field effective linewidth would be expected to decrease with increasing field as one moves away from FMR and out of the spin wave manifold regime to some high field limiting value. The ΔH_F values at the highest fields in each graph do scale with the square of the disk thickness, as was the case for the barium ferrite disk high field effective linewidth measurements of Ref. 6. Here, however, the actual ΔH_F values in the two graphs differ by a factor of 3. As an additional complication, the results were also found to depend on the disk radius R. Similar results were found for measurements at 19.3 and 35.3 GHz as well. These results show very clearly that the high field effective linewidth is not a suitable measure of the intrinsic microwave magnetic losses in these Zn-Y materials. As will be shown in the next section, eddy current losses associated with the FMR tail response, rather than magnetic losses, can account for all of the measured frequency and Q

Downloaded 26 Dec 2001 to 129.82.140.114. Redistribution subject to AIP license or copyright, see http://ojps.aip.org/japo/japcr.jsp

changes with static field, microwave orientation, disk thickness, and disk radius.

IV. ECT LOSS ANALYSIS

This section summarizes the theory for the eddy current losses associated with the FMR tail response data for the Zn-Y disk samples discussed above. The basic assumption is that eddy current losses dominate the response and that losses of a purely magnetic origin can be neglected entirely. This assumption is justified from the very large ΔH_F values shown in Fig. 6 relative to the intrinsic high field effective linewidth values found for low conductivity manganese substituted barium ferrite single crystal disks.[14] Those intrinsic values were on the order of 0.3 Oe/GHz, well below the 5–150 Oe/GHz values evident from Fig. 6. The analysis follows the same approach used in Ref. 6 for c-plane barium ferrite disks magnetized perpendicular to the disk plane. The algebra is somewhat more complicated because of the in-plane static field and magnetization direction, the elliptical $\mathbf{m}$ response with both in-plane and out-of-plane components, and the lower symmetry.

The geometry of the problem, shown in Fig. 3, was discussed in Sec. III. The uniform microwave field $\mathbf{h}(t)=\mathbf{h}e^{i\omega t}$ is assumed to drive the uniform mode dynamic magnetization $\mathbf{m}(t)=\mathbf{m}e^{i\omega t}$ specified by Eqs. (2)–(8). The $\mathbf{h}(t)$ and $\mathbf{m}(t)$ combine to produce a dynamic magnetic induction $\mathbf{b}(t)$ which induces a microwave electric field $\mathbf{e}(\mathbf{r},t)$ inside the sample. This electric field, in turn, generates eddy currents which give rise to ohmic losses. Insofar as the part of these losses which are dependent on the static magnetic field $H_{\rm ext}$ derives from the $\mathbf{m}(t)$ response associated with the tail of the usual FMR response, these eddy current losses also constitute an FMR eddy current absorption tail. As the analysis shows, it is this eddy current loss tail which is the source of the measured changes in cavity Q with $H_{\rm ext}$ presented and discussed in Sec. III. The critical assumption in the model is that the additional microwave fields produced by the eddy currents are small relative to $\mathbf{h}(t)$ and do not appreciably modify the uniform mode $\mathbf{m}(t)$ response which drives the loss tail in the first place.

Just as the high effective linewidth parameter ΔH_F served as a fitting parameter for the tail response analysis for the magnetic loss problem, the microwave conductivity σ will be the applicable fitting parameter for the eddy current loss tail. In contrast with the magnetic loss analysis, however, it is possible to obtain consistent conductivity results over the entire range of frequencies, fields, sample dimensions, and microwave orientations examined. These results indicate that the analysis of high field FMR ECT response data for magnetic materials of moderate conductivity provides a useful way to measure microwave conductivity.

It is important to emphasize that the model is valid only in the far-from-resonance limit and is useful for materials with conductivities which are not too high or too low. For high conductivity materials, the eddy current fields will be large and a full self-consistent solution of boundary value response problem based on the magnetic torque equation of motion and Maxwell's equations would be needed. Such solutions are well established for a variety of FMR and related phenomena.[15]

The electric fields and corresponding eddy current distribution for the in-plane magnetized disk geometry are best calculated in the (r,ϕ,x) cylindrical coordinate system shown in the bottom diagram of Fig. 3. The disk surfaces are at $x=\pm T/2$. The r and ϕ axes are in plane, with the r axis at an angle ϕ relative to the positive y direction and the ϕ axis at ϕ relative to the z direction. It is assumed that x-directed currents are suppressed by the thin disk geometry, i.e., the x components of the induced electric fields and currents are neglected.

One starts with the uniform microwave field $\mathbf{h}(t)=he^{i\omega t}\mathbf{x}$ or $\mathbf{h}(t)=he^{i\omega t}\mathbf{y}$ for the P and I configurations, respectively, and the corresponding dynamic magnetization $\mathbf{m}(t)=\mathbf{m}e^{i\omega t}$ responses given in Sec. III. The $\mathbf{x}$ and $\mathbf{y}$ denote unit vectors in the x and y directions, respectively. The electric field is then written as $\mathbf{e}(\mathbf{r},t)=\mathbf{e}(\mathbf{r})e^{i\omega t}$. The electric field spatial function $\mathbf{e}(\mathbf{r})$ may be obtained from Maxwell's equations according to

$$\nabla\times\mathbf{e}(\mathbf{r})=-\frac{i\omega}{c}\,\mathbf{b}, \tag{15}$$

where c is the speed of light and $\mathbf{b}$ is given by

$$\mathbf{b}=\mathbf{h}+4\pi\mathbf{m}-4\pi N_{\perp}m_x\mathbf{x}-4\pi N_{\parallel}m_y\mathbf{y}. \tag{16}$$

Note that $\mathbf{b}$ defines the time dependent magnetic induction $\mathbf{b}(t)=\mathbf{b}e^{i\omega t}$ inside the sample and contains demagnetizing terms as well as the applied microwave field $\mathbf{h}$ term and the $\mathbf{m}$ response term. For the geometry of Fig. 3, one obtains complex electric field amplitude components given by

$$e_r(\mathbf{r})=\frac{i\omega}{2c}\,(2b_y x\,\sin\phi) \tag{17}$$

and

$$e_\phi(\mathbf{r})=-\frac{i\omega}{2c}\,(b_x r-2b_y x\,\cos\phi). \tag{18}$$

Note that the electric field has both r and ϕ components, and that $\mathbf{e}(\mathbf{r})$ depends on r, ϕ, and x. This $\mathbf{e}(\mathbf{r})$ is much more complicated that the induced electric field for the perpendicular magnetized disk in Ref. 6. The vector electric field given by Eqs. (17) and (18) also satisfies the $\nabla\cdot\mathbf{e}(\mathbf{r})=0$ condition. From Ohm's law, the microwave electric field $\mathbf{e}(\mathbf{r})e^{i\omega t}$ generates an microwave current density distribution $\mathbf{j}(\mathbf{r})e^{i\omega t}=\sigma\mathbf{e}(\mathbf{r})e^{i\omega t}$, where σ denotes the microwave conductivity at frequency ω.

Let the time averaged eddy current power dissipation for the disk be denoted by P_E. This power dissipation may be obtained by integrating the time averaged eddy current power dissipation density $\frac{1}{2}\sigma|\mathbf{e}(\mathbf{r})|^2$ over the entire volume of the disk. One obtains

$$P_E=\frac{1}{2}\int_0^R\int_0^{2\pi}\int_{-T/2}^{+T/2}\sigma(|e_r(\mathbf{r})|^2+|e_\phi(\mathbf{r})|^2)r\,dr\,d\phi\,dx$$

$$=V\frac{\sigma\omega^2}{8c^2}\left(\frac{R^2}{2}|b_x|^2+\frac{T^2}{3}|b_y|^2\right), \tag{19}$$

Downloaded 26 Dec 2001 to 129.82.140.114. Redistribution subject to AIP license or copyright, see http://ojps.aip.org/japo/japcr.jsp

where the sample volume $V=\pi R^2 T$ has been explicitly factored out. Insofar as the $|b_x|^2$ and $|b_y|^2$ factors in Eq. (19) derive from a *uniform* microwave field and *uniform* dynamic magnetization response throughout the disk volume, these factors are constant. This means that the average eddy current dissipation density has additive terms which scale with the *square* of the disk radius R and the *square* of the disk thickness T. This thickness dependence is consistent with the scaling in the losses with T^2 obtained in Sec. III. Such a thickness dependence was also obtained from the barium ferrite measurements in Ref. 6. The R dependence in Eq. (19) is a new result. As will be shown below, this dependence is also borne out experimentally.

The remainder of the formal analysis is straightforward and involves writing $|b_x|^2$ and $|b_y|^2$ in terms of the microwave field and the various magnetic response functions for the I and P configurations. For the problem at hand, the microwave field is linearly polarized, of amplitude h, and along either the x axis for configuration P or along the y axis for configuration I. This means that $|b_x|^2$ and $|b_y|^2$ contain common h^2 factors which may be separated out. The end result is a working equation for the time averaged eddy current power dissipation in the disk.

$$P_E=V\frac{\sigma\omega^2 h^2}{8c^2}\left(\frac{R^2}{2}U_x+\frac{T^2}{3}U_y\right). \tag{20}$$

The U_x and U_y represent real and positive functions. These functions are different for the P and I microwave configurations. For the P configuration, U_x and U_y are given by

$$U_{XP}=1+2(1-N_\perp)4\pi\chi_x'+(1-N_\perp)^2 \times[(4\pi\chi_x')^2+(4\pi\chi_x'')^2], \tag{21}$$

and

$$U_{YP}=(1-N_\parallel)^2[(4\pi\kappa')^2+(4\pi\kappa'')^2]. \tag{22}$$

For the I configuration, U_x and U_y are given by

$$U_{XI}=(1-N_\perp)^2[(4\pi\kappa')^2+(4\pi\kappa'')^2], \tag{23}$$

and

$$U_{YI}=1+2(1-N_\parallel)4\pi\chi_y'+(1-N_\parallel)^2[(4\pi\chi_y')^2+(4\pi\chi_y'')^2]. \tag{24}$$

While the above expressions appear formidable, in the high field range well above ferromagnetic resonance which is pertinent here, they simplify considerably. In this limit the $4\pi\chi_{x,y}'$ and $4\pi\kappa'$ terms are much bigger than the $4\pi\chi_{x,y}''$ and $4\pi\kappa''$ terms. With the $4\pi\chi_{x,y}''$ and $4\pi\kappa''$ terms neglected, moreover, the resulting square bracket term in Eq. (20) becomes an absorption tail-like function of $H_{\rm ext}$, much like the $X_{QP,QI}$ functions of Sec. III. Now, however, the absorption tail reflects the eddy current losses which are driven by the real $4\pi\chi_{x,y}'$ and $4\pi\kappa'$ magnetization response terms rather that the magnetic losses considered in Sec. III. As will be shown below, it is possible to analyze the experimental $1/Q$ vs $H_{\rm ext}$ tail response data in terms of an eddy current tail and determine the microwave conductivity, in much the same way that the magnetic loss analysis yields an effective linewidth. The eddy current analysis, however, yields conductivity values which are consistent for the P and I measurements and do not depend on the static magnetic field, the disk thickness T, or the disk radius R. In order to perform such an analysis, a connection between $1/Q$ and the eddy current losses is needed. This connection is obtained below. The results of the analyses for the Zn-Y data will be presented in Sec. IV.

There is one additional difference between the eddy current losses expressed by Eqs. (20)–(24) and the magnetic loss tail response of Sec. III. This difference is in the leading "1" terms contained in the U_{XP} and U_{YI} expressions of Eqs. (21) and (24). These leading 1 terms correspond to background eddy current losses in the disk due to the eddy current induced by the applied microwave field alone. These loss contributions are independent of field and contribute to the high field limit Q value Q_N from Sec. III. Note that the U_x function has the leading 1 term for the P configuration, while the U_y function has the leading 1 for the I configuration. From the form of Eq. (20), this means that the applicable $1/Q_N$ parameter has a contribution which scales with R^2 for the P configuration measurements and a contribution which scales with T^2 for the I configuration measurements. These dependences will provide an additional way to use the $1/Q$ data to determine the microwave conductivity.

The connection between the time averaged eddy current dissipation developed above and the cavity frequency and cavity Q changes measured in the experiment can be obtained by taking advantage of the corresponding connection for magnetic dissipation and $1/Q$ already shown in Eq. (10) and the well-known basic relation between the time averaged magnetic power dissipation P_M and the magnetic response. In the present notation, this latter relation may be written as[16]

$$P_M=V\frac{\omega h^2}{8\pi}(4\pi\chi_{x,y}''), \tag{25}$$

where $4\pi\chi_x''$ is used for the P configuration and $4\pi\chi_y''$ is used for the I configuration. The combination of Eqs. (10) and (25) leads to a direct connection between $1/Q$ and magnetic loss. Equation (25), moreover, has much the same form as Eq. (20). Both contain a factor Vh^2. If the contribution of magnetic losses to the change in $1/Q$ is ignored, one can take advantage of the above connections and write an equation equivalent to Eq. (13) for eddy current losses.

$$\left(\frac{1}{Q(H_{\rm ext})}-\frac{1}{Q_N}\right)=2K_{\rm cav}\left(\frac{\sigma\omega\pi}{c^2}\right)\left(\frac{R^2}{2}U_x+\frac{T^2}{3}U_y\right). \tag{26}$$

For convenience, the combination of parameters in parenthesis in Eq. (26) is defined as a conductivity parameter G.

$$G=\frac{\sigma\omega\pi}{c^2}. \tag{27}$$

Note that in Gaussian units, conductivity is in units of s^{-1} and the G parameter has units of cm^{-2}.

It is important now to take into account the field independent 1 terms in the U_{XP} function of Eq. (21) for the P configuration and the U_{YI} function of Eq. (24) for the I configuration. Because of these terms, the value of $1/Q$ in the limit of high field will not be simply $1/Q_N$, but will contain

Downloaded 26 Dec 2001 to 129.82.140.114. Redistribution subject to AIP license or copyright, see http://ojps.aip.org/japo/japcr.jsp

an additional contribution due to the eddy current losses induced in the disk due to the microwave field $h(t)=he^{i\omega t}$ alone. The final working equation for the analysis of the $1/Q$ data takes different forms for the P and the I configuration experiments. The result for the P configuration is

$$\left(\frac{1}{Q(H_{\rm ext})}-\frac{1}{Q_{CP}}\right)=2K_{\rm cav}GX_{CP}, \tag{28}$$

with the high field tail X parameter X_{CP} given by

$$X_{CP}=\frac{R^2}{2}(U_{XP}-1)+\frac{T^2}{3}U_{YP} \tag{29}$$

and $1/Q_{CP}$, the high field limiting value for $1/Q$, given by

$$\frac{1}{Q_{CP}}=\frac{1}{Q_N}+K_{\rm cav}GR^2. \tag{30}$$

The result for the I configuration is

$$\left(\frac{1}{Q(H_{\rm ext})}-\frac{1}{Q_{CI}}\right)=2K_{\rm cav}GX_{CI}, \tag{31}$$

with the high field tail X parameter X_{CI} given by

$$X_{CI}=\frac{R^2}{2}U_{XI}+\frac{T^2}{3}(U_{YI}-1) \tag{32}$$

and $1/Q_{CI}$, the high field limiting value for $1/Q$, given by

$$\frac{1}{Q_{CI}}=\frac{1}{Q_N}+\frac{2}{3}K_{\rm cav}GT^2. \tag{33}$$

Equations (28)–(33) provide the basis for the ECT data analysis procedure described below. The overall procedure is the same as in Sec. III for the effective linewidth analysis and in Ref. 6 for the barium ferrite ECT analysis. One starts with the different sets of measurements of $Q(H_{\rm ext})$ and $\omega(H_{\rm ext})$ vs $H_{\rm ext}$ for the I and P experiments for the three nominal cavity frequencies of 10, 19.3, and 35.3 GHz. One then uses Eqs. (28)–(30) for the P configurations and Eqs. (31)–(33) for I configurations, and plots the appropriate P or I measurement set of $1/Q(H_{\rm ext})$ values obtained for a given cavity as a function of X_{CP} or X_{CI}. Note that X_{CP} and X_{CI} contain T and R as well as dependences on γ, $4\pi M_s$, H_A, $N_\perp$, $N_\parallel$, $H_{\rm ext}$, and $\omega(H_{\rm ext})$ through the $4\pi\chi'_{x,y}$ and $4\pi\kappa'$ terms in the $U_{XI,YI,XP,YP}$ expressions in Eqs. (21)–(24). Recall that at high field, $4\pi\chi'_{x,y}$ and $4\pi\kappa'$ are much bigger than $4\pi\chi''_{x,y}$ and $4\pi\kappa''$, so that the $4\pi\chi''_{x,y}$ and $4\pi\kappa''$ contributions to $U_{XI,YI,XP,YP}$ may be neglected. Recall also $N_\perp$ and $N_\parallel$ also depend on T and R. According to Eqs. (28) and (31), such plots should be linear and the slopes should be equal to $2K_{\rm cav}G$. By dividing these slopes by the slopes of the corresponding $\omega(H_{\rm ext})$ vs X_{FP} or X_{FI} plots already discussed in Sec. III, one obtains numerical values for the conductivity parameter G. These G values will be frequency band specific because of the ω factor in Eq. (27). They may be converted to conductivity from the relation

$$\sigma(\Omega^{-1}\ {\rm cm}^{-1})=\frac{G({\rm cm}^{-2})}{2\pi^2\omega({\rm GHz})}. \tag{34}$$

In Eq. (34), ω(GHz) denotes the nominal cavity frequency, in GHz. It does not represent the set of $\omega(H_{\rm ext})$ values used for the various plots. The conductivity values obtained from the above prescription is in the often used mixed units of inverse ohm centimeters.

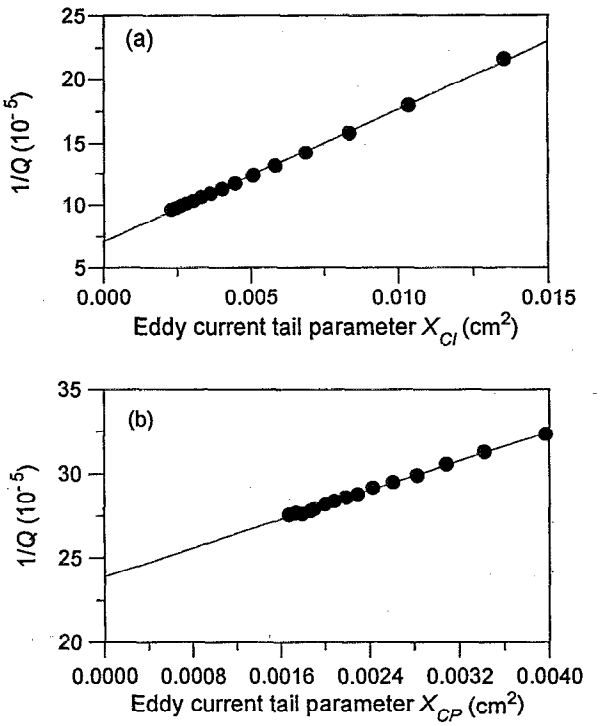

FIG. 7. Plots of $1/Q$ vs the off-resonance eddy current tail X parameters X_{CI} and X_{CP} for the 10 GHz cavity and the same 1.14-mm-thick and 3.0-mm-diam single crystal c-plane Zn-Y disk used for Fig. 4. The static external magnetic field was in plane. For (a), the microwave field was in plane and perpendicular to the static field. For (b), the microwave field was perpendicular to the disk plane. The solid lines represent linear best fits to the data.

Finally, one can also use the extrapolated $1/Q$ values from the $1/Q(H_{\rm ext})$ vs X_{CP} or X_{CI} plots at $X_{CP,CI}=0$ to obtain σ values. From Eqs. (28) to (33), these extrapolated $1/Q$ values should correspond to $1/Q_{CP}$ or $1/Q_{CI}$. These extrapolated $1/Q_{CP}$ and $1/Q_{CI}$ values should be linear functions of $K_{\rm cav}R^2$ or $K_{\rm cav}T^2$ according to Eqs. (30) and (33). The slopes of these linear plots should have slopes equal to G and extrapolated values equal to $1/Q_N$ at $K_{\rm cav}R^2=0$ or $K_{\rm cav}T^2=0$. These slopes provide a second determination of conductivity.

V. ECT ANALYSIS AND MICROWAVE CONDUCTIVITY FOR Zn-Y DISKS

This final section presents the results of the ECT analysis and summarizes the ECT conductivity values for the Zn-Y disk measurements at 10–35 GHz. The measurements and procedural details for the ECT analysis were as described above.

Figure 7 shows plots of $1/Q$ as a function of X_{CI} and X_{CP}. The plots are based on the $Q(H_{\rm ext})$ and $\omega(H_{\rm ext})$ vs $H_{\rm ext}$ data for the I and P setups with the 10 GHz cavity and the same Zn-Y disk with $T=1.14$ mm and $D=3.0$ mm featured in Figs. 4 and 5 and discussed in detail in Sec. III. Figure 7(a) is for the I configuration and Fig. 7(b) is for the P

Downloaded 26 Dec 2001 to 129.82.140.114. Redistribution subject to AIP license or copyright, see http://ojps.aip.org/japo/japcr.jsp

configuration. These plots, unlike the plots in Fig. 5, are linear over the entire range of fields used for the measurements. The slopes of the straight line fits in Figs. 7(a) and 7(b) are $0.01060 \pm 0.000\,08$ and 0.0215 ± 0.0003 cm^{-2}, respectively. These linear plots provide an indication that the ECT analysis of Sec. IV is indeed applicable to the present measurements. It is noteworthy that the actual values of the slopes are significantly different. This indicates that the effective conductivities for the I and P comfigurations are significantly different as well. The fitted slopes from Fig. 7 and the K_{cav} values from Fig. 4 yield values for the G parameter and corresponding values for the conductivity at 10 GHz. The applicable K_{cav} values of -9.63 and -10.6×10^{-4} for the I and P configurations were given in Sec. III. One then obtains σ values of 0.028 and 0.051 Ω^{-1} cm^{-1} for the I and P configurations at 10 GHz respectively. Plots similar to those in Fig. 7 were obtained for the other disks and the other measurement frequencies. The fitted conductivity values tended to increase with frequency and the P configuration generally gave higher values than did the I configuration. This increase in conductivity with frequency and the higher conductivity for the P configuration will be considered at the end of this section.

Turn now to the further analysis of the Q data in terms of the T and R dependences of the extrapolated values of $1/Q$ at $X_{CI}=0$ and $X_{CP}=0$ as described at the end of the last section. One first uses I configuration data for a range of samples of different thicknesses and obtain extrapolated values of $1/Q$ at $X_{CI}=0$ from plots similar to Fig. 7(a) for all of those samples. These extrapolated $1/Q$ values are expected to correspond to the $1/Q_{CI}$, parameter in Eq. (33). Accordingly, a plot of these empirical $1/Q_{CI}$, values vs $K_{cav}T^2$ should have a slope equal to G and a further extrapolated value at $K_{cav}T^2=0$ of $1/Q_N$. In a similar manner, one uses P configuration data for samples with different radii, obtains extrapolated values for $1/Q_{CP}$, at $X_{CP}=0$ for all of these samples, and then plots these $1/Q_{CP}$, values vs the appropriate $K_{cav}R^2$ parameter. This plot should also have a slope equal to G and a further extrapolated value at $K_{cav}R^2=0$ of $1/Q_N$.

The results of such analyses are shown in Fig. 8, based on measurements at 10 GHz. Figure 8(a) shows a plot of $1/Q_{CI}$ vs $K_{cav}T^2$ for the five disks of different thicknesses in the I configuration. The plot shows a reasonable linear dependence for a derived plot of extrapolated values. The intercept at $K_{cav}T^2=0$ corresponds to $Q_N \approx 25\,000$, which is close to the Q of the 10 GHz cavity with no sample in place. The slope of the linear best fit to the data in Fig. 8(a) gives a conductivity of 0.024 Ω^{-1} cm^{-1}. Figure 8(b) shows a plot of $1/Q_{CP}$ vs $K_{cav}R^2$ for the five disks of different radii in the P configuration. This plot also shows a reasonable linear dependence. The intercept at $K_{cav}R^2=0$ also corresponds to $Q_N \approx 25\,000$, the same as for Fig. 8(a). The slope of the linear best fit to the data in Fig. 8(b) gives a P configuration conductivity of 0.047 Ω^{-1} cm^{-1}. These values are about the same as the single sample values discussed above. They also show the same trend, with a P configuration conductivity which is larger than the I configuration value. Plots similar to those in Fig. 8 were obtained for the other disks and the other

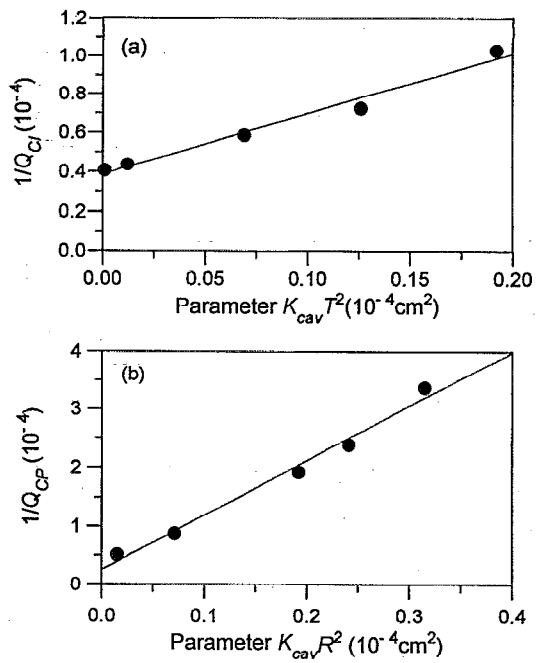

FIG. 8. Plots of (a) the high field limit $1/Q_{CI}$ values from the I configuration measurements vs the parameter $(K_{cav}T^2)$ and (b) the high field limit $1/Q_{CP}$ values from the P configuration measurements vs the parameter $(K_{cav}R^2)$ for the 10 GHz cavity. The solid lines represent linear best fits to the data.

measurement frequencies. As with the fits based from the $1/Q$ vs X_{CI} and X_{CP} plots of the sort shown in Fig. 7, the conductivity values extracted from the dependences of the extrapolated $1/Q$ values on $K_{cav}T^2$ or $K_{cav}R^2$ tended to increase with frequency and the P configuration generally gave higher values than did the I configuration. These effects will be discussed shortly.

Figure 9 summarizes all of the conductivity determinations made as described above at 10, 19.3, and 35.3 GHz.

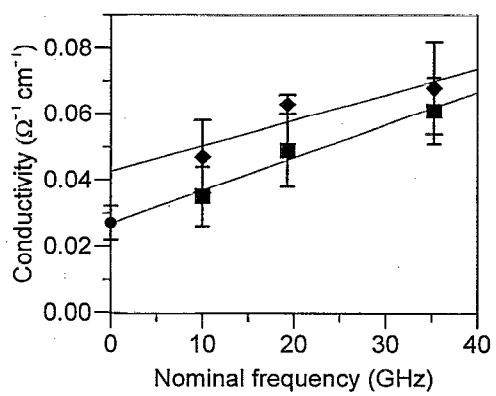

FIG. 9. Plot of experimental values of the microwave conductivity vs nominal frequency for the Zn-Y disk samples. The square and diamond symbols are for the I and P configuration measurements based on the fitted $1/Q$ vs X_{CI} or X_{CP} slopes for the individual sample measurements. The error bars indicate standard deviations for the individual sample measurements at a given frequency. The circle and error bars on the vertical axis shows the range of measured dc conductivity values for the disks.

Downloaded 26 Dec 2001 to 129.82.140.114. Redistribution subject to AIP license or copyright, see http://ojps.aip.org/japo/japcr.jsp

The solid circle and error bars on the vertical axis of the graph at zero frequency shows the results of four point probe dc conductivity measurements. The square symbols show the conductivity determinations for the I configuration and the diamond symbols show corresponding results for the P configuration. Only results from the $1/Q$ vs X_{CI} are shown. The error bars represent standard deviations for the measurements on the different samples at a given frequency. The two straight lines in the figure represent linear best fits the experimental points.

The high frequency σ values in Fig. 9 range from 0.03–0.05 $\Omega^{-1}\,\mathrm{cm}^{-1}$ at 10 GHz to 0.06–0.07 $\Omega^{-1}\,\mathrm{cm}^{-1}$ at 35 GHz. The I configuration data extrapolate to a zero frequency conductivity which is close to the measured values. The P configuration data give values which are about 10%–15% higher. The conductivity values are the same order of magnitude as measured by Kasami *et al.*[17] The behavior in Fig. 9 is about the same as found for barium ferrite in Ref. 6. Physical origins of the conductivity as well as possible dielectric loss effects are discussed in Ref. 6. The basic processes involve Fe^{3+} ions and residual Fe^{2+} ions in the crystal. Losses occur as a result of electron hopping[18,19] between equivalent lattice sites containing Fe^{3+} and Fe^{2+} ions with a characteristic hopping time T_{hop}. Such hopping processes give rise to a linear dependence of the conductivity on frequency.

VI. SUMMARY AND CONCLUSION

Microwave cavity frequency and Q measurements were made on disks of single crystal Zn-Y material at 10–35 GHz for in-plane magnetized samples and static magnetic field values well above the ferromagnetic resonance field value for a given frequency. Measurements were done for two microwave field configurations, one with the linearly polarized microwave field in the plane of the disks and one with the microwave field perpendicular to the disk plane. These two configurations gave very different results in terms of the change in Q with field. A conventional high field effective linewidth analysis of the data in terms of magnetic losses gave anomalous and inconsistent results. The high field effective linewidth values inferred from the data and the analyses changed with disk thickness, disk diameter, static magnetic field, and microwave configuration. The data were then analyzed in terms of eddy current losses. A model was developed in which the usual insulator magnetic response is used to generate currents and these currents then give rise to ohmic losses which produce a FMR ECT or ECT response. The predictions of this simple model was in good agreement with the data. The analysis yielded reasonable and consistent values for the microwave conductivity as a function of frequency.

ACKNOWLEDGMENTS

This work was supported in part by the United States Office of Naval Research, Grant N00014-90-J-4078 and the United States Army Research Office, Grant No. DAAL03-91-G-0327. The Zn-Y single crystal materials were provided by Dr. M. A. Wittenauer of Purdue University. Professor S. Shtrikman, Weitzmann Institute of Science, and Professor F. J. Friedlaender, Purdue University, initially suggested the possibility of eddy current losses as a linewidth source in hexagonal ferrite. The hard direction hysteresis curve extrapolation procedure to determine anisotropy fields was suggested by Professor J. Nyenhuis of Purdue University. Professor C. Vittoria, Northeastern University, is acknowledged for helpful advice on the shaping of disk samples for microwave and millimeter wave measurement. Professor R. E. Eykholt provided critical comments on the eddy current theory. Dr. M. Mendik, Dr. M. A. Tsankov, Dr. M. Chen, J. M. Nash, and M. J. Hurben provided a critical reading of the manuscript.

[1] C. E. Patton, in *Magnetic Oxides*, edited by D. J. Craik (Wiley, London, 1975), p. 575.
[2] M. V. Kogekar and C. E. Patton, J. Magn. Magn. Mater. **54**, 1139 (1986).
[3] W. D. Wilber and L. Silber, J. Appl. Phys. **63**, 3353 (1988).
[4] K. D. McKinstry, C. E. Patton, M. A. Wittenauer, M. Sankararaman, J. Nyenhuis, F. J. Friedlaender, H. Sato, and A. Schindler, IEEE Trans. Magn. **MAG-25**, 3482 (1989).
[5] R. Karim, K. D. McKinstry, J. R. Truedson, and C. E. Patton, IEEE Trans. Magn. **MAG-28**, 3225 (1992).
[6] J. R. Truedson, K. D. McKinstry, P. Kabos, and C. E. Patton, J. Appl. Phys. **74**, 2705 (1993).
[7] D. O. Smith, in *Magnetism*, edited by G. T. Rado and H. Suhl (Academic, New York, 1965), Vol. 3, p. 465.
[8] E. Schlömann, T. Kohane, and J. J. Green, Technical Report No. AFML-TR-67-201 (1967).
[9] M. A. Wittenauer, J. A. Nyenhuis, A. I. Schindler, H. Sato, F. J. Friedlaender, J. R. Truedson, R. Karim, and C. E. Patton, J. Cryst. Growth **130**, 533 (1993).
[10] J. A. Osborn, Phys. Rev. **67**, 351 (1945).
[11] M. Sugimoto, in *Ferromagnetic Materials*, edited by E. P. Wohlfarth (North-Holland, Amsterdam, 1982), Vol. 3, p. 382.
[12] B. Lax and K. J. Button, *Microwave Ferrites and Ferrimagnetics* (McGraw–Hill, New York, 1962), p. 150.
[13] J. J. Green and T. Kohane, SCP Solid State Tech. **7**, 46 (1964).
[14] R. Karim, S. D. Ball, J. R. Truedson, and C. E. Patton, J. Appl. Phys. **73**, 4512 (1993).
[15] J. F. Cochran, B. Heinrich, and G. Dewar, Can. J. Phys. **55**, 787 (1977).
[16] A. Yariv, *Quantum Electronics* (Wiley, New York, 1989), p. 86.
[17] A. Kasami and S. Koide, J. Phys. Soc. Jpn. **21**, 552 (1966).
[18] M. Sparks, *Ferromagnetic Relaxation* (McGraw–Hill, New York, 1964), p. 107.
[19] R. Parker, in *Magnetic Oxides*, edited by D. J. Craik (Wiley, London, 1975), p. 439.

Downloaded 26 Dec 2001 to 129.82.140.114. Redistribution subject to AIP license or copyright, see http://ojps.aip.org/japo/japcr.jsp